Optimization of assembly clamping pressure on performance of proton-exchange membrane fuel cells

Xiu Qing Xing*, Kah Wai Lum, Hee Joo Poh, Yan Ling Wu

Institute of High Performance Computing, 1 Fusionopolis Way, #16-16 Connexis, Singapore 138632, Singapore

ABSTRACT

The compression induced by the assembly of proton-exchange membrane (PEM) fuel cells causes partial deformation of the gas-diffusion layers (GDLs) and affects the characteristics of the porous media and, consequently, influences the performance of PEM fuel cells. The objective of the present study is: (1) to develop a three-dimensional model to investigate the effect of assembly clamping pressure on the GDL properties and thus on the performance of PEM fuel cells, and (2) to determine the optimum clamping pressures when the cell is operated under different operating voltages. The optimum clamping pressures under different operating voltages are explored by using a global searching method, namely, the simultaneous perturbation stochastic algorithm (SPSA) method. The simulation results indicate that a clamping pressure of 1 or 1.5 MPa improves the fuel cell performance when the cell is operated under high operating voltages, and causes the cell performance to decrease when it is operated under low-voltage conditions. The optimum clamping pressures increase when the operating voltage increases.

© 2009 Published by Elsevier B.V.

1. Introduction

Much attention has been paid to the membranes and the active layers in proton-exchange membrane (PEM) fuel cells, whereas little focus has been placed on the gas distribution layer (GDL) although it plays a crucial role in the cells. The GDL links the bipolar plates and the active layers, provides mechanical support, supplies reactants to the active layers, collects the current, and removes heat and water from the membrane. Therefore, changes in the physical properties of the GDLs may have significant effects on cell performance.

The properties of GDLs, such as thickness, porosity/permeability and conductivity, are highly sensitive to the clamping pressure since GDLs are typically made of highly porous carbon-fibre paper or cloth. The contact resistance between the GDLs and the current-collectors, and the contact resistance between the GDLs and the active layers, also change with the clamping force. Consequently, the clamping pressure has a strong impact on fuel cell performance due to the concomitant changes in GDL properties and contact resistances.

Recently, more and more experimental and numerical studies have been conducted to explore the effect of GDL deformation on the PEM fuel cell performance [1–3]. Experimental studies by Gostick et al. [3] have indicated that the compression of a sample to half its initial thickness results in a decrease in in-plane permeability by an order of magnitude. Mishra et al. [4] reported experimental data to show the effects of different GDL materials and clamping pressures on the electrical contact resistance. Lee et al. [5] conducted experimental studies of the performance of PEM fuel cells with different types of GDL materials and found that the optimum clamping pressure is different for different GDL materials. Cho [6] examined the effects of different bipolar plate materials on the contact resistance by experimental measurements. Davies [7] presented experimental data for the effects of the compaction force on interfacial ohmic losses. Babcock et al. [8] investigated the trade-off between lateral mass transport resistance losses and cathode–GDL contact resistance losses. Nitta et al. [9] found that the inhomogeneous compression of GDLs may lead to significant local variations of mass and charge transport properties in GDLs. Hottinen et al. [10] modelled the effects of inhomogenous compression of a GDL on mass and charge transport in a PEM fuel cell. Zhou et al. [11–13] simulated the effects of GDL compression deformation and ohmic contact resistance on the performance of the PEM fuel cells.

It is well known that the PEM fuel cell components are held together under certain clamping forces mainly to prevent gas leakages. High clamping forces will decrease the porosity/permeability of the GDLs, and cut down gas diffusion to the reactive layers and, consequently, reduce the cell performance. On the other hand, high clamping pressure can also decrease the contact resistance between the GDLs and the current-collectors/active layers, and increase GDL electrical conductivity, there by improving the cell performance. Therefore, a balance between porosity and

* Corresponding author. Tel.: +65 64191323; fax: +65 64191580.
E-mail address: xingxq@ihpc.a-star.edu.sg (X.Q. Xing).

Nomenclature

A	cross-sectional area through which the force is applied
c	concentration of the species (mol m^{-3})
D	diffusion coefficient (m^2 s^{-1})
E_{eq}	equilibrium voltage (V)
$\mathbf{F}$	body force (N)
F	Faraday's constant (96,487 A s mol^{-1})
h	GDL thickness (m)
Δh	change amount of the GDL thickness (m)
j	transfer current density (A m^{-2})
j_o	exchange current density (A m^{-2})
M	molecular mass (kg mol^{-1})
N	mass flux (kg m^{-2} s^{-1})
p	pressure (Pa)
p_f	clamping pressure (Pa)
Q	source term of mass balance equations (kg m^{-3} s^{-1})
r	contact resistance
R	gas constant (J mol^{-1} K^{-1})
R^{agg}	agglomerate radius (m)
s	specific area (m^{-1})
S	current source term (A m^{-3})
$\mathbf{u}$	velocity vector (m s^{-1})
$\mathbf{X}$	design variable vector
x,y	coordinates (m)

Greek letters

x	mole fraction
$\boldsymbol{\Delta}$	perturbation vector
ϕ	potentials (V)
ε	porosity
η	dynamic viscosity (N s m^{-2})
η_v	overvoltage (V)
κ	permeability (m^2)
λ	Lagrange multiplier
σ	conductivity (S m^{-1})
ρ	mixture density (kg m^{-3})
ω	mass fraction

Subscript

a	anode
c	cathode
H$_2$	hydrogen
H$_2$O	water
in	in-plane
k	counter index
m	membrane
min	minimum
O$_2$	oxygen
s	electrode
th	through-plane
0	without deformation

Superscript

agg	agglomerate
ref	reference
T	temperature

ohmic resistance determines the cell performance due to GDL deformation. Motivated by this knowledge, a three-dimensional multi-physics model is developed in this study to investigate and optimize the effect of clamping pressure on cell performance. Searching for the optimum clamping pressures for PEM fuel cells operated under different operating voltages is carried out by means of a global optimization method, namely, a simultaneous perturbation stochastic algorithm (SPSA) [14–16].

2. Modelling with COMSOL^{TM} multi-physics

Modelling an air-breathing PEM fuel cell is a challenge since the process is a multi-physics phenomenon that involves mechanical deformation of the GDLs, electrochemical reactions, flow dynamics in the gas channels, and heat and mass transport in porous media. In this study, a steady-state, single-phase, three-dimensional model for an air-breathing PEM fuel cell is developed with COMSOL^{TM} multi-physics to simulate the performance of the cell, which is considered as the objective function in the optimization studies.

An air-breathing PEM fuel cell is shown schematically in Fig. 1(a). A typical computational domain is selected as a repetitive unit of the PEM fuel cell surrounded by the dashed line, as shown in Fig. 1(a). The whole computational domain consists of a membrane, GDLs on the cathode and the anode sides, an air-breathing slot, a hydrogen channel, and current-collectors on both sides, as shown in Fig. 1(b). The catalyst layers at both the anode and the cathode are simplified as boundaries between the GDLs and the membrane; the thickness of the catalyst layers is accounted in the membrane's dimensions. Air is induced into the cathode channels by means of natural convection, whereas hydrogen is delivered into anode channel through forced convection. The pressures of both the air and the hydrogen are set at one standard atmosphere. The assumptions used in the model include:

1. The membrane and catalyst layers are stiff, and no deformation occurs with clamping pressure.
2. There is no leakage under the clamping pressures considered.
3. The GDL is assumed to be isotropic and the in-plane deformation is ignored since it has insignificant effects on the cell performance according to Zhou et al. [12].
4. Water in the fuel cell exists as vapour. The electrodes and membrane are made of homogeneous materials with uniform morphological properties.
5. The cell is considered to be isothermal, i.e., the temperature distribution across the cell is uniform.
6. Humified air is considered on the cathode side while only hydrogen and water vapour are considered on the anode side.

The multi-component diffusion and convection phenomena are described by the Maxwell-Stafen equation, which has the following general form.

$$\frac{\partial}{\partial t}\rho\omega_i + \nabla \cdot \left[-\rho\omega_i \sum_{j=1}^{N} D_{ij}\left\{ \frac{M}{M_j}\left(\nabla\omega_j + \omega_j\frac{\nabla M}{M}\right) + (x_j - \omega_j)\frac{\nabla p}{p}\right\} \right.$$
$$\left. + \omega_i\rho\mathbf{u} + D_i^T\frac{\nabla T}{T}\right] = Q_i \tag{1}$$

where D_{ij} is the diffusion coefficient, D^T is the multi-component thermal diffusion coefficient, Q_i is the source term, x is the species mole fraction, ω is the species mass fraction, T is the temperature, and M stands for the molecular mass. Temperature-driven diffusion is insignificant due to an assumed uniform temperature and therefore the source term Q_i is set to zero.

On the cathode side, two transport equations are solved to obtain the mass fractions of oxygen and water; the mass fraction of nitrogen can be obtained from the mass balance equation:

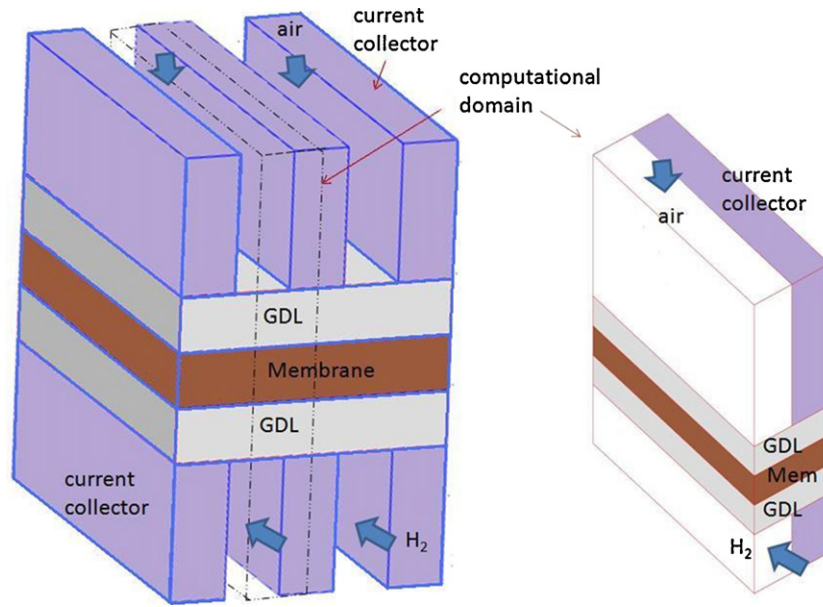$$\omega_{N_2} = 1 - \omega_{O_2} - \omega_{H_2O} \tag{2}$$

Fig. 1. Scheme of (a) air-breathing PEM fuel cell and (b) computational domain.

Similarly, on the anode side, the transport equation of hydrogen is solved and the mass fraction of water can be obtained by:

$$\omega_{H_2O} = 1 - \omega_{H_2} \tag{3}$$

The deformation ($\Delta h(x,y)$) of the GDLs can be calculated using the definition of the Young's modulus.

$$E = \frac{F/A_0}{\Delta h(x,y)/h_0} \tag{4}$$

E is the Young's modulus, F is the clamping force, A_0 is the original cross-sectional area through which the clamping force applied, h_0 stands for the original thickness of the GDL, and $\Delta h(x,y)$ is the amount of change of the GDL thickness. Consequently, the deformation of the GDL thickness is $\Delta h(x,y) = Fh_0/EA_0$, and the GDL thickness distribution will be $h(x,y) = h_0 - \Delta h(x,y)$.

It is assumed that the deformation under compression is due to a change in the volume of pores, not in the volume of bulk material. Thus, the porosity (ε) of the GDL can be evaluated through the change in the thickness of the GDL, i.e.,

$$\varepsilon(x,y) = \varepsilon_0 \frac{h(x,y) - h_{min}}{h_0 - h_{min}} \tag{5}$$

where h_{min} stands for the minimum thickness when there is no pore volume left in the GDL, and $h_{min} = (1 - \varepsilon_0)h_0$.

The velocity distribution in the porous media of the GDL is formulated by Darcy's law, namely,

$$u = -\frac{\kappa(x,y)}{\eta} \nabla p \tag{6}$$

where η is the dynamic viscosity and $\kappa(x,y)$ is the permeability, which varies non-linearly as the compressed thickness of the GDL decreases. The value of $\kappa(x,y)$ is obtained through fitting a third-degree polynomial function to the measured permeability data [9], which are based on SIGRACET GDL carbon paper (made by SGL Carbon Group). The third-degree polynomial function is:

$$\kappa(x,y) = -1.700 \times 10^{-11} + 2.760 \times 10^{-7} h(x,y)$$
$$- 1.484 \times 10^{-3} h^2(x,y) + 2.754 h^3(x,y) \tag{7}$$

At the electrode/membrane boundary, the mass fluxes of hydrogen in the anode (N_{H_2}), and of oxygen (N_{O_2}) and water (N_{H_2O}) in the

cathode, are determined by the following reaction rates, respectively:

$$N_{H_2} = -\frac{j_a}{2F} M_{H_2}$$
$$N_{O_2} = -\frac{|j_c|}{4F} M_{O_2} \tag{8}$$
$$N_{H_2O} = \frac{|j_c|}{2F} M_{H_2O}$$

where j_a and j_c are the transfer current density corresponding to electrochemical reaction at the anode and cathode catalyst layers.

The agglomerate model describes the current density in an active layer consisting of agglomerates of ionic conductor material and electrically conducting particles covered partially with catalyst. The governing equations for the current density in the anode and cathode are:

$$j_a = -\frac{6(1-\varepsilon)FD_H^{agg}}{(R^{agg})^2} \left(c_H^{agg} - c_H^{ref} \exp\left(-\frac{2F}{RT}\eta_v\right) \right)$$
$$\times \left(1 - \sqrt{\frac{j_{o,a}s}{2Fc_H^{ref}D_H^{agg}}} R^{agg} \coth \sqrt{\frac{j_{o,a}s}{2Fc_H^{ref}D_H^{agg}}} R^{agg} \right)$$

$$j_c = R\frac{12(1-\varepsilon)FD_O^{agg}}{(R^{agg})^2} c_O^{agg} \left(1 - \sqrt{\frac{j_{o,c}s(R^{agg})^2}{4Fc_O^{ref}D_O^{agg}}} \exp\left(-\frac{0.5F}{RT}\eta_v\right) \right)$$
$$\times \coth \sqrt{\frac{j_{o,c}s(R^{agg})^2}{4Fc_O^{ref}D_O^{agg}}} \exp\left(-\frac{0.5F}{RT}\eta_v\right) \tag{9}$$

where D^{agg} is the agglomerate gas diffusivity; R is the gas constant; R^{agg} is the agglomerate radius; s is the specific area of the catalyst inside the agglomerate; F is the Faraday constant; c^{ref} and c^{agg} are the concentrations of the reference species and that of the agglomerate surface; j_o is the exchange current density; T is the temperature. Finally, the overvoltage η_v is defined as $\eta_v = \phi_s - \phi_m - E_{eq}$, where ϕ_s and ϕ_m are the potentials in the electrode and in the membrane, respectively. E_{eq} is the equilibrium voltage.

The direct current application mode for conductive media describes the potential distribution in the solid-phase GDL and in

the membrane using the following equations:

$$\nabla \cdot (-\sigma_{s,eff} \nabla \phi_s) = S_s$$
$$\nabla \cdot (-\sigma_{m,eff} \nabla \phi_m) = S_m$$
(10)

where S_s and S_m are the current source terms in the solid phase and the electrolyte phase, respectively; $\sigma_{s,eff}$ is the solid-phase effective electronic conductivity; $\sigma_{m,eff}$ is the membrane ionic conductivity. The GDL in-plane and through-plane conductivities are modelled as function of the thickness of the GDL, as in Hottinen et al. [10], i.e.,

$$\sigma_{s\text{-in}}(x, y) = 6869 - 1.159 \times 10^7 h(x, y)$$
$$\sigma_{s\text{-th}}(x, y) = 3285 - 8.385 \times 10^6 h(x, y)$$
(11)

The loss of potential between the GDL and the current-collector is due to the contact resistance. Here, the contact resistance r is evaluated based on a fitted function for the experimental data of Mishra et al. [4] for bipolar plates made from graphite, i.e.,

$$r = 3.32 \times 10^{-7}(1.01 \times 10^6/p_f)^{0.534} \quad \text{for SGL-10-BA}$$
$$r = 3.72 \times 10^{-7}(0.966 \times 10^6/p_f)^{0.692} \quad \text{for SGL-10-BB}$$
(12)

The potentials of the GDL and the current-collectors are related to each other through the current passing the interface between the GDL and the current-collectors, i.e.,

$$i = \frac{(\phi_{s\text{-collector}} - \phi_{s\text{-GDL}})}{r}$$
(13)

3. Optimization method

The SPSA method is selected to perform the optimization search because of its powerful search ability and relative ease of implementation. The essential feature of SPSA is the underlying gradient approximation, which requires only two measurements of the objective function to approximate the gradient regardless of the dimension of the optimization problem. This feature results in a significant decrease in the computational cost of the optimization.

The problem of minimizing a scalar differentiable loss function $L(\mathbf{X})$, where $\mathbf{X}$ is a p-dimensional vector of design variables, can be treated as searching for the vector $\mathbf{X}^*$ such that $\partial L/\partial \mathbf{X}^* = 0$. This is the classical formulation of local optimization for differentiable loss functions and it is assumed that measurements of $L(\mathbf{X})$ are available for various values of $\mathbf{X}$. The SPSA algorithm is usually defined in the general recursive stochastic algorithm form, i.e.,

$$\mathbf{X}_{k+1} = \mathbf{X}_k - a_k g(\mathbf{X}_k)$$
(14)

where $g(\mathbf{X}_k)$ is the estimate of the gradient $\partial L/\partial \mathbf{X}$ at the iteration k based on measurements of the loss function. For a two-sided simultaneous perturbation, the approximation of the gradient is given as:

$$g(\mathbf{X}_k) = \frac{y(\mathbf{X}_k + c_k \mathbf{\Delta}_k) - y(\mathbf{X}_k - c_k \mathbf{\Delta}_k)}{2c_k} \begin{bmatrix} \Delta_{k1}^{-1} \\ \Delta_{k2}^{-1} \\ \vdots \\ \Delta_{kp}^{-1} \end{bmatrix}$$
(15)

The parameter $c_k = c_0/(k^m)$, where c_0 is a small positive number and m is a coefficient which is assigned a value of 1/6 in this study. The term $\mathbf{\Delta}_k$ represents the random perturbation vector generated by Monte Carlo approaches and the components of this perturbation are independently generated from a zero-mean probability distribution. One simple distribution that has been used in this study is the Bernoulli ± 1 distribution with probability of 0.5 for each ± 1 outcome.

Table 1
Geometry and functional parameters.

Description	Value
Anode GDL thickness	0.25 mm
Cathode GDL thickness	0.25 mm
Thickness of the membrane and catalyst layers	0.25 mm
Height of the anode channel	0.5 mm
Height of the cathode channel	1.2 mm
Anode exchange current density	1000 A m^{-2}
Cathode exchange current density	0.1 A m^{-2}
Faraday's constant	96487 C mol^{-1}
Membrane conductivity	9 S cm^{-1}
Solid-phase conductivity	1000 S cm^{-1}
Permeability	10^{-13} m^2
Anode electrode potential	0 V

The SPSA algorithm starts from an initial guess of the optimum vector $\mathbf{X}_0$. First, the counter index k is initialized to a value of 0. Then an initial guess of the design variable vector $\mathbf{X}_k$ and the non-negative empirical coefficients are defined. Next, a p-dimensional random simultaneous perturbation vector $\mathbf{\Delta}_k$ is constructed and two measurements of the objective function, namely, $y(\mathbf{X}_k + c_k \mathbf{\Delta}_k)$ and $y(\mathbf{X}_k - c_k \mathbf{\Delta}_k)$, are obtained based on the simultaneous perturbation around the given vector $\mathbf{X}_k$. Then the simultaneous perturbation approximates to the gradient $g(\mathbf{X}_k)$ using Eq. (15). This is followed immediately by updating of the design vector $\mathbf{X}_k$ to a new value $\mathbf{X}_{k+1}$ using the general recursive stochastic algorithm form, $\mathbf{X}_{k+1} = \mathbf{X}_k - a_k g(\mathbf{X}_k)$, where the parameter $a_k = a_0/(A + k)^\alpha$; a_0, A, and α can be chosen to ensure an effective practical performance of the algorithm. In this study, $a_0 = 0.167$, $A = 1$, and α is set as 1. Finally, the algorithm is terminated if there are insignificant changes in several successive iterations, or if the maximum allowable number of iterations has been reached. The details of the step-by-step implementation of the SPSA algorithm have been explained by Spall [14–16]. The choice of the coefficients and parameters pertaining to the algorithm is crucial to the performance of the SPSA. Some useful guidelines for choosing the values of these coefficients and parameters can be found in references [14–19].

In this study, the optimization problem is solved using the SPSA method to maximize the average current density at the cathode side. The objective function is evaluated by running the 3D COMSOL^{TM} model under the MATLAB^{TM} environment.

4. Results and discussion

Two carbon paper-based GDLs (SGL-10-BA and SGL-10-BB, made by SGL Carbon Group) are used for the studies with the following two objectives: (a) to study the effects of GDL deformation on the physical properties of the GDLs and the contact resistance between the GDLs and the current-collectors, and consequently the effect on fuel cell performance, and (b) to determine the optimum clamping pressures corresponding to different operating voltages.

The fuel cell is operated at 353 K and one standard atmosphere pressure. The geometric parameters, such as the dimensions of the different components and the functional parameters, are listed in Table 1.

4.1. Effect of GDL deformation on fuel cell performance

The Young's moduli of the carbon paper-based GDLs (SGL-10-BA and SGL-10-BB) reported in Mishra et al. [4] are listed in Table 2. The data clearly show that the moduli have three regions identified under different clamping pressures. The deformation of the GDLs under different clamping pressures is shown in Fig. 2. It can be seen that the deformation of the GDL increases piecewise linearly when the clamping pressure increases since the Young's modulus of the GDL changes piecewise linearly, as listed in Table 2.

Table 2
Compressive modulus of SGL carbon paper-based GDL.

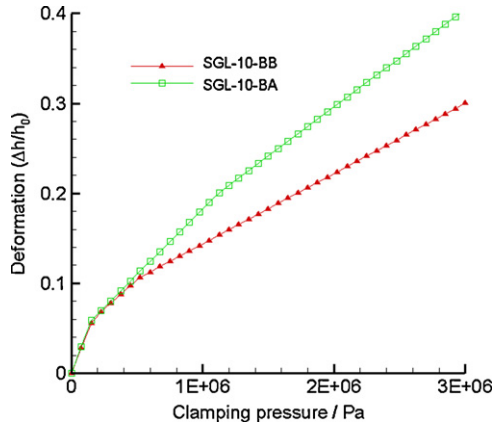| Material	Pressure range (MPa)	E (MPa)
SGL-10-BA	0.00–0.15	1.71
	0.15–1.12	4.59
	1.12–3.00	6.16
SGL-10-BB	0.00–0.16	1.81
	0.16–0.52	5.11
	0.52–3.00	8.57

Fig. 2. Deformation of GDLs.

When the clamping pressure is as high as 3 MPa, the corresponding deformations are 30.0% and 40.5% of the initial GDL thickness with SGL-10-BB and SGL-10-BA as the GDLs, respectively.

Fig. 3 quantitatively shows the change in the electric conductivity of the GDL versus the clamping pressure. Similar trends are
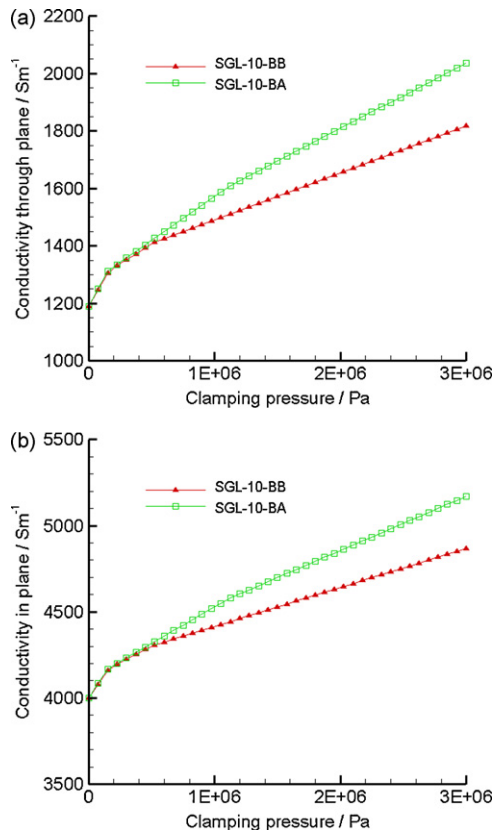

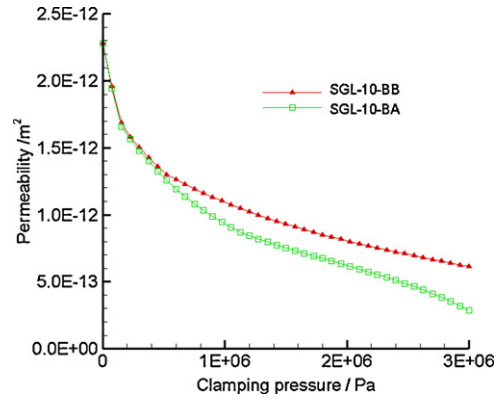**Fig. 3.** Conductivities (a) through-plane conductivity and (b) in-plane conductivity.

Fig. 4. Permeabilities of GDLs.

found in the change of the through-plane and in-plane conductivities of the GDLs under the effect of clamping pressures, i.e., conductivities non-linearly increase with increasing the clamping pressures. For example, when the clamping pressure increases from 0 to 3 MPa, the through-plane conductivity increases by 52.9% with SGL-10-BB as the GDLs, and the through-plane conductivity of SGL-10-BA is raised by 71.3%, where as the in-plane conductivities increase 21.7% and 29.3% for SGL-10-BB and SGL-10-BA, respectively. From the data in Fig. 3, it can be concluded that SGL-10-BB is much stiffer than SGL-10-BA.

The change in permeability when the clamping pressure changes is presented in Fig. 4. A converse trend is found as compared with the conductivities. Permeability reduces with increasing clamping pressure due to a reduction in the void spaces in the GDLs for the fluid transmission. With the clamping pressure increasing from 0 to 3 MPa, the permeability non-linearly reduces by 69.5% and 87.5% for SGL-10-BB and SGL-10-BA, respectively.

The electric contact resistances between the GDL and the current-collectors depend strongly on the compression pressure. In this study, the electric contact resistance is approximated as a function of the compressed GDL thickness, which is shown in Eq. (12). Fig. 5 compares the fitted and the measured contact resistance between the GDL and the current-collectors. From Fig. 5, it can be seen that the fitted contact resistances have a good agreement with the measured data reported in Mishra et al. [4], and the contact resistance reduces all the way from small clamping pressures to high clamping pressures.

Clamping effects on fuel cell performance are studied based on SGL-10-BB as the GDL material of the fuel cell. For a fuel cell without considering the clamping pressure, i.e., there is no deformation of the GDLs, and no changes on either the porosity/permeability
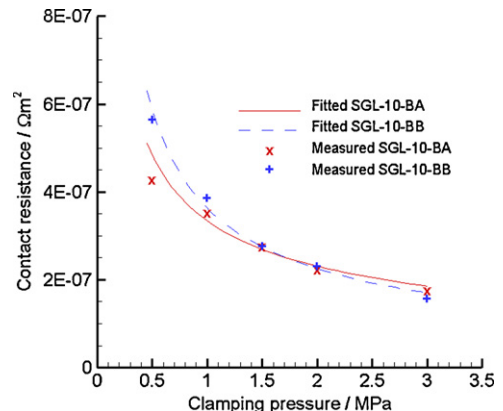

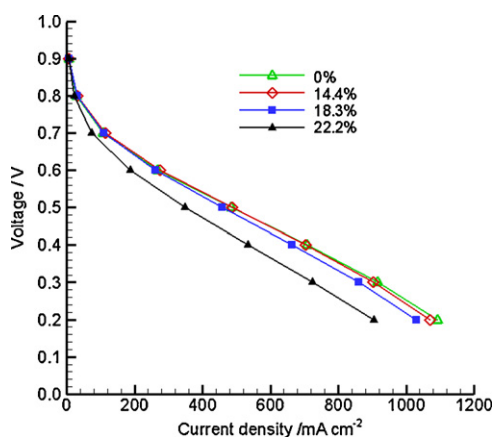**Fig. 5.** Contact resistances between GDLs and current-collectors.

Fig. 6. Polarization curves with different GDL deformations.

or the conductivity, the contact resistances between the GDLs and the current-collectors are assumed to be a constant. For a fuel cell with clamping pressures applied, the deformation, porosity/permeability and conductivity of the GDLs, and the contact resistances between the GDLs and the current-collectors are evaluated using the method described in Section 2. It is assumed that there is no leakage of the reactants for all these cases.

Fig. 6 compares the polarization curves obtained with different clamping pressures. Clamping pressures are given as 0, 1, 1.5 and 2.0 MPa, and the corresponding GDL deformations are 0%, 14.4%, 18.3% and 22.2% of the GDL initial thickness, respectively. From Fig. 6, it can be seen that with a GDL deformation of 14.4% and 18.3% (corresponding to the clamping pressures of 1 and 1.5 MPa), the fuel cell performances indicated by the average current densities are worse than that without any deformation when the cells are operated in a low-voltage region. Conversely, the performances of the fuel cells with 14.4% and 18.3% GDL deformations become better than that without any deformation when the cells are operated in a high-voltage region. This scenario can be explained as follows: when there is no clamping pressure, the contact resistance between the GDL and the current-collectors is higher compared with the case with a clamping pressure applied. High contact resistance stands for high ohmic resistance, low current density, and hence worse cell performance. Meanwhile, the porosity/permeability of the GDLs without any clamping pressure is higher than that with a clamping pressure applied. High porosity/permeability allows for more reactant supply to the active layer, and thus improves cell performance. As previously mentioned, the balance between these two factors determines the cell performance. When the fuel cell works in a high-voltage region, the chemical reaction rate is low, and the cell does not demand a large amount of reactant. Therefore, the effect of the contact resistance on cell performance is dominant over the effect of porosity/permeability. Accordingly, clamping pressures of 1 and 1.5 MPa result in lower contact resistances and sufficient reactant supplies, and there by better cell performances in a high-voltage region. By contrast, the chemical reaction rate is high when the fuel cell works in a low-voltage region, causing the

cell to demand large amount of reactant. Therefore, the effect of the porosity/permeability dominates that of the contact resistance. As a result, no clamping pressure applied on the GDL stands for high porosity and high reactant supply to the chemical reaction, and presents better cell performances in a low-voltage region.

The data in Fig. 6 also indicate that the performance of the fuel cell with 22.2% GDL deformation is significantly worse than that without any clamping pressure, especially in a low-voltage region. This suggests that a clamping pressure of 2.0 MPa is too high for the fuel cell to achieve its optimum performance. From Fig. 6, it can be concluded that the optimum clamping pressure varies with the operating condition, and the optimum pressures under different operating conditions for the fuel cell described in this study should be less than 2.0 MPa.

4.2. Optimal clamping pressures under different operating voltages

Searching for the optimum clamping pressures under different operating voltages has been carried out for two different paper-based GDLs, namely, SGL-10-BA and SGL-10-BB. The cell performance is indicated by the average current density and is set as the objective function, and the clamping pressure is selected as the design variable, which is subjected to the lower and upper boundaries. The SPSA method is adopted to maximize the average current densities under the prescribed operating voltages.

Table 3 presents the optimization results of the two cases with SGL-10-BA and SGL-10-BB as the GDL materials, respectively. It can be clearly seen that the optimum clamping pressures corresponding to the best average current density increase with increasing the operating cell voltages for both the GDL materials. For example, when SGL-10-BB is used as the GDL, the optimum clamping pressure is found to be 0.7782 MPa, and the corresponding average current density is 111.656 mA cm^{-2}, at an operating voltage of 0.7 V; the optimum clamping pressure is 0.3694 MPa when the operating voltage is 0.4 V, and the corresponding current density is 709.750 mA cm^{-2}. Similarly, when SGL-10-BA is employed as the GDLs, the optimum clamping pressure is reduced from 0.2689 to 0.1310 MPa when the operating voltage is decreased from 0.7 to 0.4 V.

The data in Table 3 suggest that the optimum clamping pressure increases when the operating voltage increases, i.e., the optimum clamping pressures at high operating voltages are higher than those at low operating voltages. All the optimum clamping pressures are less than 1.0 MPa. This is consistent with the findings from the comparison of the cell performances under different clamping pressures. The reason for the phenomena can be similarly explained as follows: assuming there is no leakage under the clamping pressures considered in this study, the chemical reaction rate is low at high voltage, thus only demanding a small amount of reactants, which makes it possible for the deformed GDLs with relatively lower porosities to supply sufficient reactants. Hence, the effect of the contact resistance on the cell performance plays a dominant role over that of porosity/permeability. Consequently, a high clamping pressure is required to obtain better performance. Conversely, low-

Table 3
Optimum clamping pressures under different operating voltages.

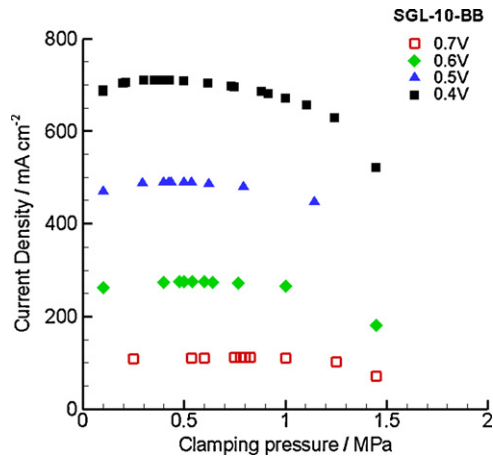| Operating voltage (V)	SGL-10-BB		SGL-10-BA	
	Optimum current density (mA cm^{-2})	Corresponding clamping pressure (MPa)	Optimum current density (mA cm^{-2})	Corresponding clamping pressure (MPa)
0.4	709.749980	0.3693667	701.191470	0.1310000
0.5	488.587082	0.4235709	482.599964	0.1503828
0.6	274.454882	0.5403518	271.619690	0.1905609
0.7	111.656020	0.7782217	110.994067	0.2688909

Fig. 7. Optimization histories for cases with SGL-10-BB as GDLs at different operating voltages.

voltage operating conditions correspond to high chemical reaction rates, thus requiring GDLs with high porosity to supply sufficient reactants for the chemical reactions. The effects of the porosities on the cell performance will overrule that of the contact resistances. As a consequence, the cell requires a low clamping pressure to obtain better performance.

In addition, Table 3 indicates that the optimum clamping pressures with SGL-10-BA as the GDLs are lower than those with SGL-10-BB. The reason is due to the fact that the Young's modulus of SGL-10-BA is smaller than that of SGL-10-BB. A lower Young's modulus indicates a softer material. Therefore, for the SGL-10-BA GDL, a small clamping force can cause a large deformation, large decreases of porosity and contact resistance, and thus, significant impacts on fuel cell performance.

Fig. 7 shows the optimization histories for fuel cell using SGL-10-BB as the GDL material and operated under different cell voltages, from 0.4 to 0.7 V. It can be seen that the optimum clamping pressure increases when the operating voltage increases. The convergence history curve becomes more and more flat with increasing operating voltage. This indicates that the cell performance becomes less sensitive to the clamping pressure at high operating voltage region. Additionally, the data in Fig. 7 suggest that the SPSA method is efficient. It searches the optimum between the lower and upper bounds of the design variable with large step sizes at a zone far away from the optimum, and small step sizes at a zone near to the optimum, to ensure a global optimum and a high searching efficiency.

5. Conclusions

A three-dimensional model to evaluate the effects of assembly clamping pressure on the GDL's porosity/permeability and conductivity of GDLs, as well as the contact resistance between the GDLs and the current-collector, has been developed. Simulation results indicate that the performance of a fuel cell operated under high operating voltages benefits from a small assembly clamping pressure. Conversely, for a cell operated in a low-voltage region, a fuel cell without clamping pressure demonstrates better performance than a cell with an assembly clamping pressure because the clamping pressure has a negative effect on the cell performance. Too high clamping pressure degrades the fuel cell performance along the entire polarization curve, i.e., in both the high-voltage and low-voltage regions.

The optimum clamping pressures under different operating voltages are explored by using the simultaneous perturbation stochastic algorithm method. The optimization results suggest that the optimum clamping pressure is different for different GDL materials, and the optimum clamping pressures corresponding to different operating voltages increase with increasing the operating voltage for both cases with SGL-10-BA and SGL-10-BB as the GDL materials. In addition, SPSA method is found to be efficient method for optimizing fuel cell performance.

References

[1] J. Ge, A. Higier, H. Liu, J. Power Sources 159 (2006) 922–927.
[2] S. Escribano, J. Blachot, J. Ethève, A. Morin, R. Mosdale, J. Power Sources 156 (2006) 8–13.
[3] J.T. Gostick, M.W. Fowler, M.D. Pritzker, M.A. Ioannidis, L.M. Behra, J. Power Sources 162 (2006) 228–238.
[4] V. Mishra, F. Yang, R. Pitchumani, J. Fuel Cell Sci. Technol. 1 (2004) 2–9.
[5] W.K. Lee, C.H. Ho, J.W. Van Zee, M. Murthy, J. Power Sources 84 (1999) 45–51.
[6] E.A. Cho, J. Power Sources 125 (2004) 178–182.
[7] D.P. Davies, J. Power Sources 86 (2000) 237–242.
[8] B. Babcock, A.J. Tupper, D. Clark, T. Fabian, R. O'Hayre, Fuel Cell 2008-65171, ASME 6th International Fuel Cell Science, Engineering & Technology Conference, June 16–18, 2008, Denver, Colorado, USA, 2008.
[9] I. Nitta, T. Hottinen, O. Himanen, M. Mikkola, J. Power Sources 171 (2007) 26–36.
[10] T. Hottinen, O. Himanen, S. Karvonen, I. Nitta, J. Power Sources 171 (2007) 113–121.
[11] P. Zhou, C.W. Wu, J. Power Sources 170 (2007) 93–100.
[12] P. Zhou, C.W. Wu, G.J. Ma, J. Power Sources 159 (2006) 1115–1122.
[13] P. Zhou, C.W. Wu, G.J. Ma, J. Power Sources 163 (2007) 874–881.
[14] J.C. Spall, IEEE Trans. Aero. Electron. Syst. 34 (1998) 817–823.
[15] J.C. Spall, Johns Hopkins APL Tech. Dig. 19 (1998) 482–492.
[16] J.C. Spall, IEEE Trans. Autom. Control 37 (1992) 332–341.
[17] V. Fabian, in: J.J. Rustigi (Ed.), Stochastic Approximation. Optimizing Methods in Statistics, Academic Press, New York, 1971, pp. 439–470.
[18] D.C. Chin, IEEE Trans. Syst. Man Cybern. 27 (1997) 244–249.
[19] J. Dippon, J. Renz, SIAM J. Control Optimization 35 (1997) 1811–1827.